Microporous and Mesoporous Materials 311 (2021) 110695

Contents lists available at ScienceDirect

Microporous and Mesoporous Materials

journal homepage: http://www.elsevier.com/locate/micromeso

Ultrastable luminescent hybrid microporous polymers based on polyhedral oligomeric silsesquioxane for CO_2 uptake and metal ion sensing

Mohamed Gamal Mohamed [a,b], Ni-Yun Liu [a], Ahmed F.M. EL-Mahdy [a], Shiao-Wei Kuo [a,c,*]

[a] Department of Materials and Optoelectronic Science, Center of Crystal Research, National Sun Yat-Sen University, Kaohsiung, 804, Taiwan
[b] Chemistry Department, Faculty of Science, Assiut University, Assiut, 71516, Egypt
[c] Department of Medicinal and Applied Chemistry, Kaohsiung Medical University, Kaohsiung, 807, Taiwan

ARTICLE INFO

Keywords:
POSS
Microporous polymers
Heck reaction
CO_2 uptake
Metal ion sensing

ABSTRACT

In this study we prepared four different fluorescent hybrid microporous polymers (HPPs) derived from cubic octavinylsilsesquioxane (OVS) through Heck coupling with brominated anthracene (An-Br_2), triphenyltriazine (TPT-Br_3), bicarbazole (Car-Br_4) and tetraphenylethene (TPE-Br_4). The chemical structures of these HPPs were confirmed using Fourier transform infrared spectroscopy and solid-state NMR spectroscopy. Thermogravimetric analysis and N_2 adsorption/desorption measurements revealed that each of these HPPs had outstanding thermal stability, a high surface area, and inherent porosity. The CO_2 uptakes of TPT-HPP and Car-HPP at 273 and 298 K were higher than those of An-HPP and TPE-HPP. Furthermore, the luminescence of these HPPs could be quenched completely upon the addition of Fe^{2+}, and Fe^{3+} metal cations. Thus, these HPP materials appear to be good candidates for CO_2 adsorption and metal ion sensing.

1. Introduction

Covalent organic porous polymers (OPPs) are emerging types of materials having two- or three-dimensional network structures, inherent porosity, high surface areas, and high total pore volumes [1–15]. They have recently attracted interest from industry and academia because of their potential applications in gas storage, heterogeneous catalysis, chemosensing, optoelectronics, light harvesting, energy conversion, hydrogen evolution, the oxygen reduction reaction, water treatment, and gas separation [16–29]. Fluorescent organic porous polymers (FPPs) are generally constructed from rigid and extended π-conjugated aromatic compounds, which enhance the porosity by inhibiting the network from collapsing and provide the materials with luminescence properties [30–33]. Many color-tunable conjugated microporous polymers (CMPs) have been prepared by introducing pyrene (Py), bicarbazole (Car), triphenylamine, tetraphenylethene (TPE), and phenyl moieties into these materials [34–37]. The most interesting property of FPPs is that their emissions are typically stronger than those of conventional conjugated polymers, presumably because their highly porous network architectures inhibit chain aggregation [5,38–41]. Although OPPs would appear to have many applications in various fields, their use remains limited because of poor thermal and mechanical properties [5].

Inorganic polyhedral oligomeric silsesquioxane (POSS, typically $R_8Si_8O_{12}$) has been used as a building block for the preparation and construction of many hybrid polymers [5,42–45]. Hybrid porous polymers derived from bulky and rigid POSS moieties have received much attention recently for their excellent chemical, mechanical, and thermal stability and flame and water retardance [42–48]. The preparation of porous POSS nanocomposite materials has been achieved using Sonogashira, hydrosilylation, Heck, Yamamoto, and Friedel–Crafts reactions [5,49–55]. In many cases, the solubility, quantum yields, and photophysical properties of polymers can be improved after the introduction of POSS units [5]. For example, Liu et al. prepared a nanoporous polymer (Py-HPP) incorporating Py and octavinylsilsesquioxane (OVS) moieties through a Friedel–Crafts reaction; it exhibited excellent adsorption uptake toward berberine chloride hydrate (BCH) [56]. Geng et al. synthesized luminescent CMPs based on TPE through reactions catalyzed by CH_3SO_3H; these materials had surface areas of up to 564 $m^2\ g^{-1}$ and displayed excellent I_2 adsorption [57]. In addition, Liu et al. prepared a series of hybrid porous materials through Friedel–Crafts reactions between TPE and OVS; these porous polymers possessed high surface areas and micro- and mesoporous structures [10]. Liu et al. also prepared two different kinds of hybrid polymers (HPP-1, HPP-2) through Heck reactions of OVS with 2,2′,7,7′-tetrabromo-9,

* Correspondence author. Department of Materials and Optoelectronic Science, Center of Crystal Research, National Sun Yat-Sen University, Kaohsiung, 804, Taiwan.
E-mail address: kuosw@faculty.nsysu.edu.tw (S.-W. Kuo).

https://doi.org/10.1016/j.micromeso.2020.110695
Received 4 August 2020; Received in revised form 29 September 2020; Accepted 13 October 2020
Available online 16 October 2020
1387-1811/

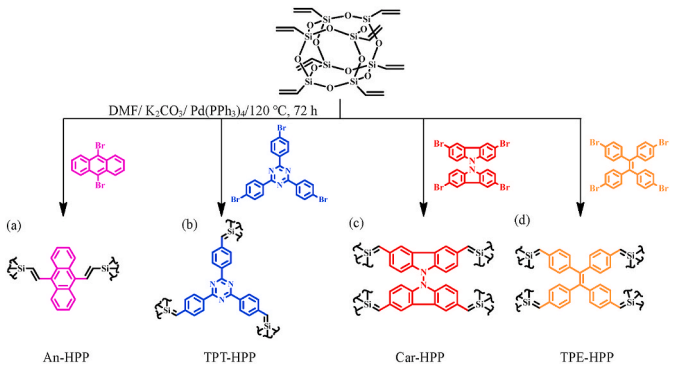

Scheme 1. Syntheses of (a) An-HPP, (b) TPT-HPP, (c) Car-HPP and (d) TPE-HPP.

9′-spirobifluorene and 1,3,6,8-tetrabromopyrene [58]. Sprick and his group prepared CMP networks based on phenyl- and pyrene-based monomers through Suzuki–Miyaura copolymerization. They found that the resulted materials exhibited different color by altering the monomer ratio, and specific monomer compositions and these materials can act as effective photocatalysts for the hydrogen production from water [59]. Xu et al. reported that CMP with highly yellow light-emitting based on tetrakis(4-bromophenyl)ethene and the resulting CMP can act as an antenna for light-harvesting [36].

In this study, we prepared four different luminescent hybrid microporous polymers (HPPs) through Heck reactions of OVS with brominated anthracene (An-Br_2), triphenyltriazine (TPT-Br_3), bicarbazole (Car-Br_4), and TPE (TPE-Br_4) [Scheme 1]. As reported, these four monomers have different planarity; for example, anthracene and triphenyl triazine are planar aromatic hydrocarbon; bicarbazole molecule is nonplanar and extended in two perpendicular positions with a torsional angle of 125°; and tetraphenylethene molecule has propeller-like, nonplanar conformations and its four phenyl rings are twisted out of the central alkene plane by ~50°. Therefore, we expect that the preparation luminescent hybrid microporous polymers containing POSS unit and these four monomers, we can obtain on porous materials with different properties such as thermal stability, porosities, morphology, and optical properties. We used Fourier transform infrared (FTIR) spectroscopy and solid-state NMR spectroscopy confirmed their chemical. We performed X-ray diffraction (XRD), the Brunauer–Emmett–-Teller (BET) method, photoluminescence (PL) spectroscopy, scanning electron microscopy (SEM), and transmission electron microscopy (TEM) to study the surface morphologies, porosities, crystallinities, and emission properties of these polymers in the solid state and in solvents of various polarities. We also applied the BET method and PL spectroscopy to examine the potential applications of these materials for CO_2 uptake and the sensing for various metal cations.

2. Experimental

2.1. Materials

Octavinylsilsesquioxane (OVS), potassium carbonate (K_2CO_3), triethylamine (Et_3N), tetrahydrofuran (THF), acetone, methanol (MeOH), dimethyl sulfoxide (DMSO), anhydrous ferric chloride ($FeCl_3$), ferrous chloride ($FeCl_2$), magnesium chloride ($MgCl_2$), zinc chloride ($ZnCl_2$) and copper(II) chloride ($CuCl_2$) were purchased from Alfa Aesar. Potassium iodide (KI) and nickel(II) chloride ($NiCl_2$) were ordered from Showa. Tetrakis(triphenylphosphine)palladium(0) [$Pd(PPh_3)_4$] was obtained from Sigma–Aldrich. *N*,*N*-Dimethylformamide (DMF) was dried at 90 °C for 12 h over CaH_2. 2,4,6-Tris(4-bromophenyl)-1,3,5-triazine (TPT-Br_3), 3,3′,6,6′-tetrabromo-9,9′-bicarbazole (Car-Br_4), and 1,1,2,2-tetrakis(4-bromophenyl)ethene (TPE-Br_4) were prepared using previously reported methods [19,22,24,29] [Scheme S1–**S4**]. The NMR spectral data of these synthesized monomers were consistent with those reported [Fig. S1–**S8**].

2.2.9,10-Dibromoanthracene (An-Br_2): In a one-neck flask, Br_2

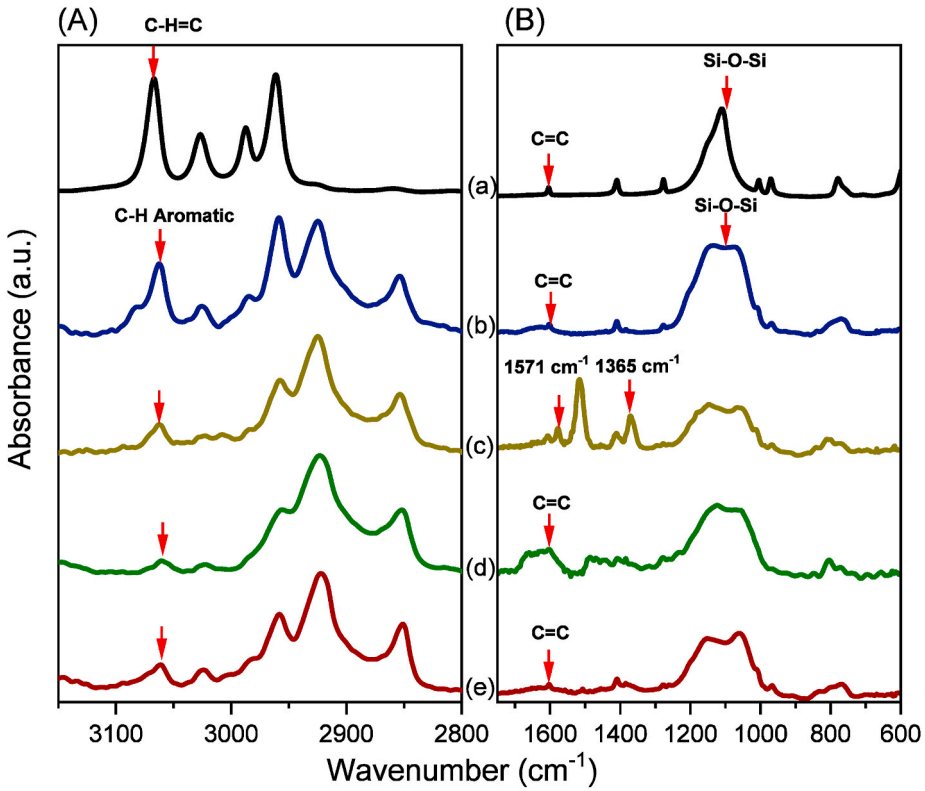

Fig. 1. FTIR spectra (recorded at 25 °C) of (a) OVS, (b) An-HPP, (c) TPT-HPP, (d) Car-HPP, and (e) TPE-HPP.

(35.8 g, 11.6 mL, 0.224 mol) was added dropwise to a solution of anthracene (20.0 g, 0.112 mol) in acetic acid (600 mL). The solution was stirred for 4 h until a yellow solid appeared. Then the yellow solid was filtered off, washed with methanol and dried at 50 °C for 24 h to afford An-Br_2 (35.4 g, 94%); mp: 220–222 °C. ^{1}H NMR (500 MHz, $CDCl_3$, δ, ppm, Fig. S1): 8.57 (4H, $ArCH_{1,4,5,8}$), 7.62 (4H, $ArCH_{2,3,6,7}$). ^{13}C NMR (125 MHz, $CDCl_3$, δ, ppm, Fig. S2). 131.63, 128.88, 128.09, 123.76.

2.3. An-HPP: OVS (1.26 g, 2.00 mmol), $Pd(PPh_3)_4$ (126 mg, 0.100 mmol), An-Br_2 (1.00 g, 40.0 mmol), K_2CO_3 (4.40 g, 32.0 mmol), and dry DMF (40 mL) were charged in a dry three-neck flask under a N_2 atmosphere. The mixture was stirred at 120 °C for 72. The precipitate was filtered off, washed sequentially with THF, water, MeOH, and acetone, and dried under reduced pressure at 90 °C for 48 h to afford An-HPP as a green solid (1 g).

2.4. TPT-HPP: OVS (1.26 g, 2.00 mmol), $Pd(PPh_3)_4$ (126 mg, 0.100 mmol), TPT-Br_3 (1.00 g, 40.0 mmol), K_2CO_3 (4.40 g, 32.0 mmol), and dry DMF (40 mL) were charged in a dry three-neck flask under a N_2 atmosphere. The mixture was stirred at 120 °C for 3 days. The precipitate was filtered off, washed sequentially with THF, water, MeOH, and acetone, and dried under reduced pressure at 90 °C for 48 h to afford TPT-HPP as a yellow solid (1.2 g).

2.5. Car-HPP: OVS (1.26 g, 2.00 mmol), $Pd(PPh_3)_4$ (126 mg, 0.100 mmol), Car-Br_4 (1.00 g, 40.0 mmol), K_2CO_3 (4.40 g, 32.0 mmol), and dry DMF (40 mL) were charged in a dry three-neck flask under a N_2 atmosphere. The mixture was stirred at 120 °C for 3 days. The precipitate was filtered off, washed sequentially with THF, water, MeOH, and acetone, and dried under reduced pressure at 90 °C for 48 h to afford Car-HPP as a brown solid (1.1 g).

2.6. TPE-HPP: OVS (1.26 g, 2.00 mmol), $Pd(PPh_3)_4$ (126 mg, 0.100 mmol), TPE-Br_4 (1.00 g, 40.0 mmol), K_2CO_3 (4.40 g, 32.0 mmol), and dry DMF (40 mL) were charged in a dry three-neck flask under a N_2 atmosphere. The mixture was stirred at 120 °C for 3 days. The precipitate was filtered off, washed sequentially with THF, water, MeOH, and acetone, and dried under reduced pressure at 90 °C for 48 h to afford TPE-HPP as a light-yellow solid (0.86 g).

Metal ion titration procedure

1 mg/mL of An-HPP, TPT-HPP, Car-HPP and TPE-HPP was prepared in ethanol solution and stored at 4 °C. Then, $FeCl_3$ was dissolved in Milli-Q water for obtaining metal ion stock solutions (10^{-2} mol/L). Afterthat, different concentrations of Fe^{3+} ions were added to an ethanol solution of An-HPP TPT-HPP, Car-HPP and TPE-HPP and mixed. Finally, the photoluminescence spectra were recorded.

3. Results and discussion

3.1. Synthesis of An-HPP, TPT-HPP, Car-HPP, and TPE-HPP

Scheme 1 displays the synthetic routes that we followed to prepare the four different POSS-based fluorescent HPPs. We obtained An-HPP, TPT-HPP, Car-HPP, and TPE-HPP through Heck reactions of OVS with An-Br_2, TPT-Br_3, Car-Br_4, and TPE-Br_4, respectively, each in dry DMF containing $Pd(PPh_3)_4$ and K_2CO_3, at 120 °C for 3 days. After the reactions had reached completion, the crude materials were washed several times with THF, H_2O, acetone, and MeOH to remove any traces of salts, catalyst, and unreacted monomers. The resulting porous polymers were insoluble in DMF, THF, CH_2Cl_2, MeOH, and acetone. We used FTIR spectroscopy and solid-state NMR spectroscopy to confirm the chemical structures of An-HPP, TPT-HPP, Car-HPP and TPE-HPP. The FTIR spectrum of OVS [Fig. 1(A) and (B)] features absorption bands at 3066, 1600 and 1107 cm^{-1}, corresponding to stretching vibrations of the C═C–H, C═C, and Si–O–Si units, respectively. The FTIR spectra of An-HPP, TPT-HPP, Car-HPP, and TPE-HPP [Fig. 1(b–e)] featured absorption signals in the range 3050–3084 cm^{-1} for stretching of their aromatic C–H units and at 1600 cm^{-1} for stretching of their C═C bonds.

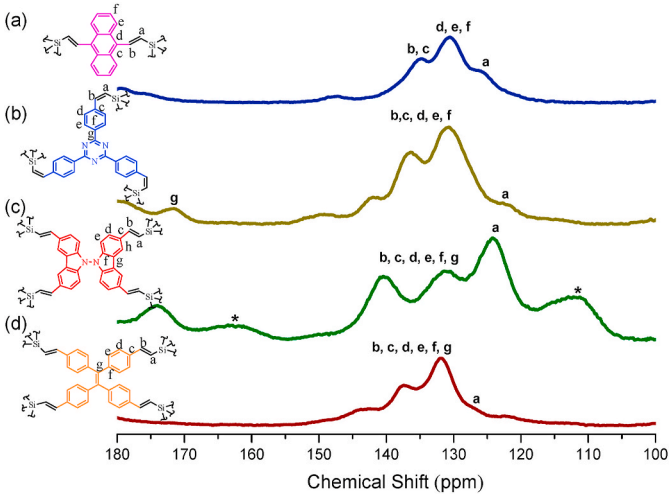

Fig. 2. Solid state ^{13}C CP/MAS NMR spectra (recorded at 25 °C) of (a) An-HPP, (b) TPT-HPP, (c) Car-HPP, and (d) TPE-HPP. Asterisks denote spinning sidebands.

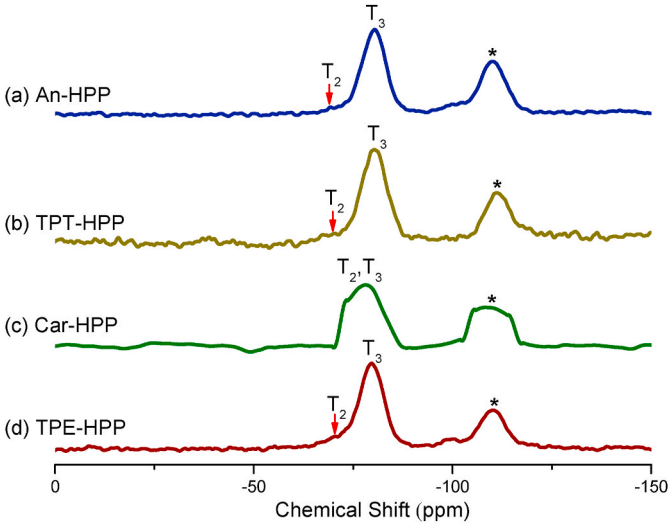

Fig. 3. Solid state ^{29}Si NMR spectra (recorded at 25 °C) of (a) An-HPP, (b) TPT-HPP, (c) Car-HPP, and (d) TPE-HPP. Asterisks denote spinning side-bands.

In addition, the spectrum of TPT-HPP [Fig. 1(c)] featured absorptions bands at 1571 and 1365 cm^{-1} representing the triazine ring. The absorption bands for Si–O–Si stretching at 1107 cm^{-1} were broader in the FTIR spectra of An-HPP, TPT-HPP, Car-HPP, and TPE-HPP than they were in the spectrum of OVS, consistent with the presence of cross-linked networks [5,58–63].

Fig. 2 presents the solid state ^{13}C CP/MAS NMR spectra of our four POSS-based fluorescent HPPs. The signals of the carbon nuclei of the SiCH═CH and SiCH═CH-Ph units were centered at 126 and 135 ppm, respectively, for An-HPP [Fig. 2(a)], at 123 and 142 ppm, respectively, for TPT-HPP [Fig. 2(b)], at 124 and 140 ppm, respectively, for Car-HPP [Fig. 2(c)], and at 127 and 138 ppm, respectively, for TPE-HPP [Fig. 2 (d)], consistent with the formation of internal olefinic bonds through the reactions of the brominated aromatic compounds and vinyl groups. We attribute the signals for An-HPP, TPT-HPP, Car-HPP, and TPE-HPP in the ranges 135–131, 136–131, 140–132, and 138–132 ppm, respectively, to the carbon nuclei of their anthracene, triazine, Car, and TPE units. In addition, a peak appeared in the spectrum of TPT-HPP at 172 ppm [Fig. 2(b)], representing the C═N moieties of its triazine units.

Furthermore, we recorded ^{29}Si MAS NMR spectra [Fig. 3(a–d)] to

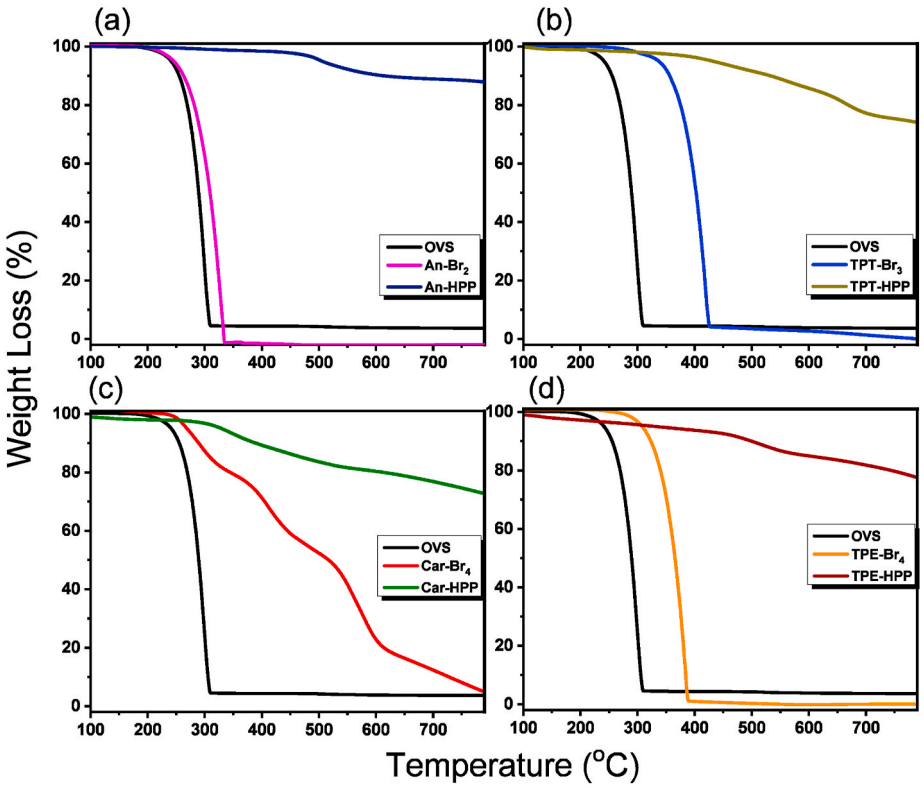

Fig. 4. TGA traces of OVS, An-Br_2, TPT-Br_3, Car-Br_4, and TPE-Br_4 and their corresponding HPPs.

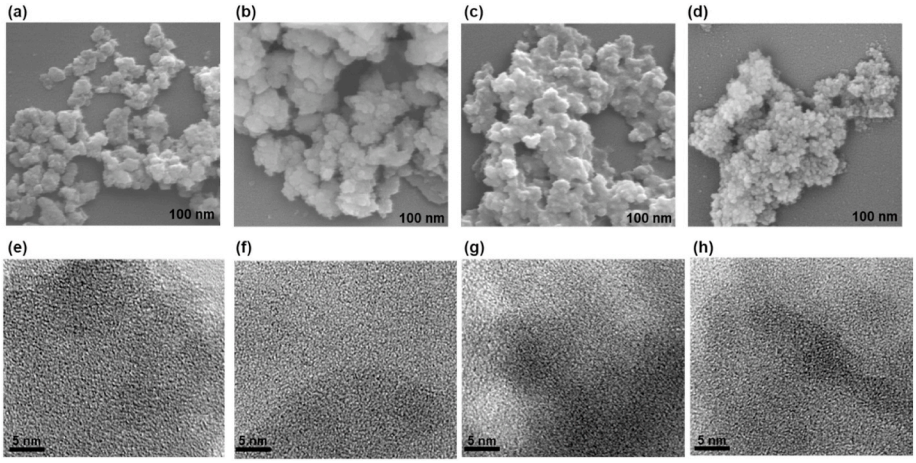

Fig. 5. (a–d)SEM and (e–h) TEM images of (a, e) An-HPP, (b, f) TPT-HPP, (c, g) Car-HPP, and (d, h) TPE-HPP.

confirm the presence of POSS units in these HPPs. Each of these spectra featured signals near 69.02 and 80.52 ppm, attributable to the presence of T_2 and T_3 units in the framework [T_n: $CSi(OSi)_n(OH)_{3-n}$]; that is, partial collapse of the POSS moieties occurred during the reaction, but POSS units remained in all of these frameworks [5,49,52]. Taken together, these spectral analyses confirmed the successful syntheses of An-HPP, TPT-HPP, Car-HPP, and TPE-HPP.

We used thermogravimetric analysis (TGA) to evaluate the thermal stability of An-HPP, TPT-HPP, Car-HPP, and TPE-HPP and their monomers (Fig. 4). OVS provided thermal degradation temperatures (T_{d5} and T_{d10}) of 246 and 263 °C, respectively, with a char yield of 3.62%. After crosslinking OVS with An-Br_2, TPT-Br_3, Car-Br_4, and TPE-Br_4, the thermal degradation temperatures and the char yields increased for all the resulting polymer frameworks. For An-HPP, the values of T_{d5} and T_{d10} and the char yield were 505 °C, 614 °C, and 88% respectively; for TPT-HPP they were 432 °C, 533 °C, and 74%, respectively; for Car-HPP they were 329 °C, 389 °C, and 73%, respectively; and for TPE-HPP they were 319 °C, 492 °C, and 77%, respectively. Thus, the An-HPP framework exhibited outstandingly high thermal stability when compared with the other frameworks, due to its rigid aromatic structure and high crosslinking density. Table S1 summarizes the values of T_{d5} and T_{d10} and the char yields for OVS, the four fluorescent monomers, and the four HPPs.

The XRD patterns of these microporous polymers (Fig. S9) did not reveal any long-range crystallographic features, suggesting amorphous character [5,49]. We used field-emission SEM (FE-SEM) and high-resolution TEM (HR-TEM) to examine the surface morphologies, ordering, and textural properties of these four polymers. The SEM images in Fig. 5(a–d) reveal that our four microporous polymers all comprised similarly shaped irregularly aggregated spherical particles having dimensions of several nanometers. The TEM images in Fig. 5

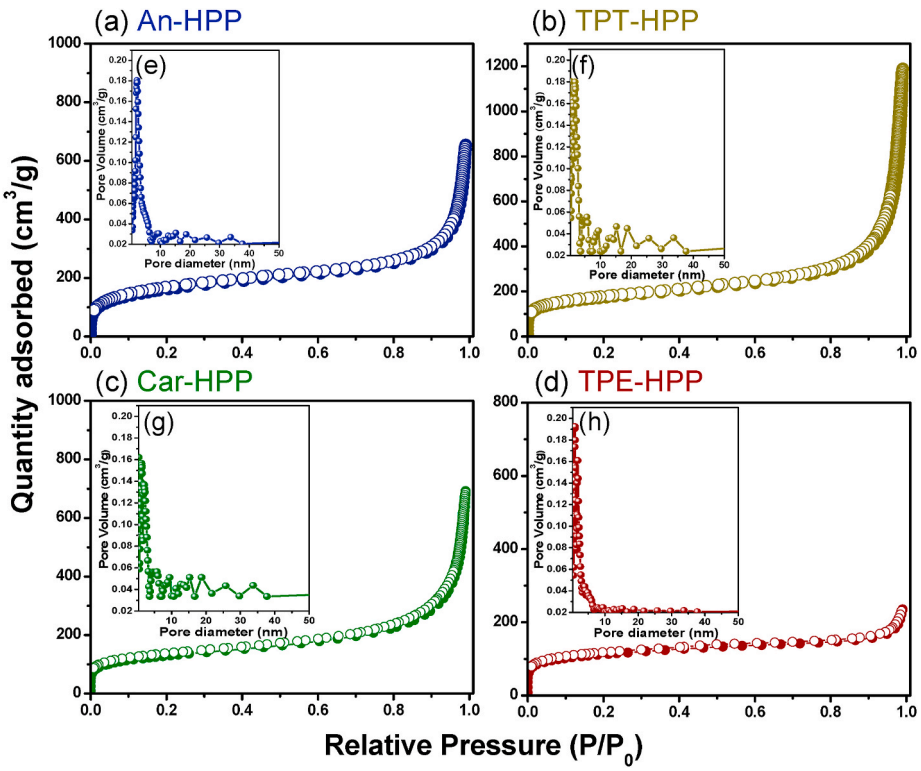

Fig. 6. (a –d) N_2 adsorption/desorption isotherms and (e–h) pore size distribution curves of (a, e) An-HPP, (b, f) TPT-HPP, (c, g) Car-HPP, and (d, h) TPE-HPP.

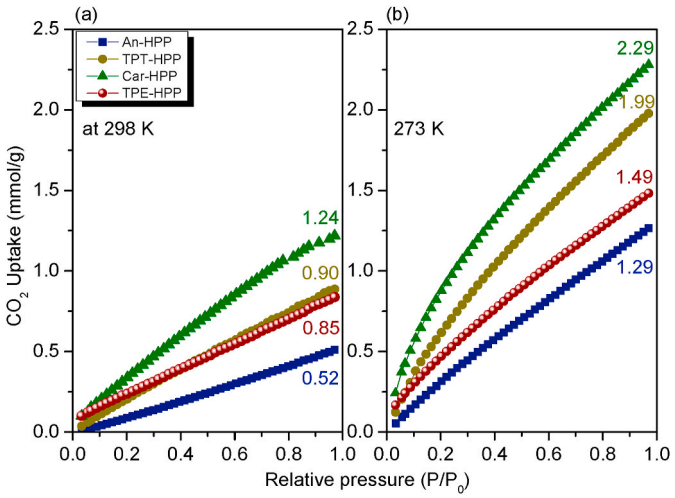

Fig. 7. CO_2 uptake isotherms of An-HPP, TPT-HPP, Car-HPP, and TPE-HPP recorded at (a) 298 and (b) 273 K.

(e–h) reveal that these polymer frameworks were microporous materials possessing uniform pore structures (<2 nm). Furthermore, the TEM images suggested that these polymer structures had no long-range order, consistent with the XRD patterns in Fig. S9.

To examine the porosity of An-HPP, TPT-HPP, Car-HPP, and TPE-HPP, we recorded their N_2 adsorption and desorption properties at 77 K (Fig. 6). Based on IUPAC classification, all of the N_2 isotherms of these polymers were of type I and II. Each N_2 isotherm exhibited a sharp N_2 uptake at low pressure and then increasing N_2 adsorption at higher relative pressure. The BET specific surface areas and total pore volumes (V_{total}) were 611 $m^2\ g^{-1}$ and 0.63 $cm^3\ g^{-1}$, respectively, for An-HPP; 626 $m^2\ g^{-1}$ and 1.83 $cm^3\ g^{-1}$, respectively, for TPT-HPP; 585 $m^2\ g^{-1}$ and 0.75 $cm^3\ g^{-1}$, respectively, for Car-HPP; and 400 $m^2\ g^{-1}$ and 0.53 $cm^3\ g^{-1}$, respectively, for TPE-HPP. We used nonlocal density functional theory (NL-DFT) to determine the pore size diameters of An-HPP, TPT-HPP, Car-HPP, and TPE-HPP [Fig. 6(e–h)]. An-HPP featured pores of two sizes, with diameters of 2.19 and 1.00 nm; the pore size distribution curves of TPT-HPP, Car-HPP, and TPE-HPP revealed narrow micropore distributions, with two average pore diameters of 1.00–9.49, 1.01–9.47, and 1.16–4.91 nm, respectively. Thus, the BET surface areas and total pore volumes of An-HPP, TPT-HPP, and Car-HPP were higher than those of TPE-HPP, presumably because of greater cross-linking densities and relatively smoother connections between the POSS units and the anthracene, triazine, and Car moieties. The pore size distribution curves [Fig. 6 (e–g)] showed that An-HPP, TPT-HPP, and Car-HPP materials contain mesoporous structures.

3.2. CO_2 uptake and metal ion sensing

Because of their high porosities (with high BET surface areas and different average pore diameters), we expected our materials to uptake CO_2. Thus, we performed CO_2 adsorption measurements at two different temperatures: 298 and 273 K [Fig. 7(a) and **7(b)**]. The CO_2 capacities of An-HPP, TPT-HPP, Car-HPP, and TPE-HPP at 298 K were 0.52, 0.90, 1.24, and 0.85 mmol g^{-1}, respectively; at 273 K, they were 1.29, 1.99, 2.29, and 1.49 mmol g^{-1}, respectively. Interestingly, the CO_2 uptakes of TPT-HPP and Car-HPP at 273 K were higher than those of An-HPP, TPE-HPP, and other porous polymers derived from 1,3,5-tribromobenzene and OVS [49,52], presumably because of the presence of triazine and Car units in the former pair. The incorporation of some functional groups (e.g., carboxyl, amino) into porous materials has been found previously to enhance CO_2 uptake [64–66]. Furthermore, Cooper et al. reported that triazine porous framework materials exhibited excellent adsorption of CO_2 when compared with corresponding benzene derivatives [67,68]. As presented in Table S2, TPT-HPP and Car-HPP displayed excellent CO_2 uptake performance when compared with the other porous materials.

We used fluorescence measurements to examine the photophysical

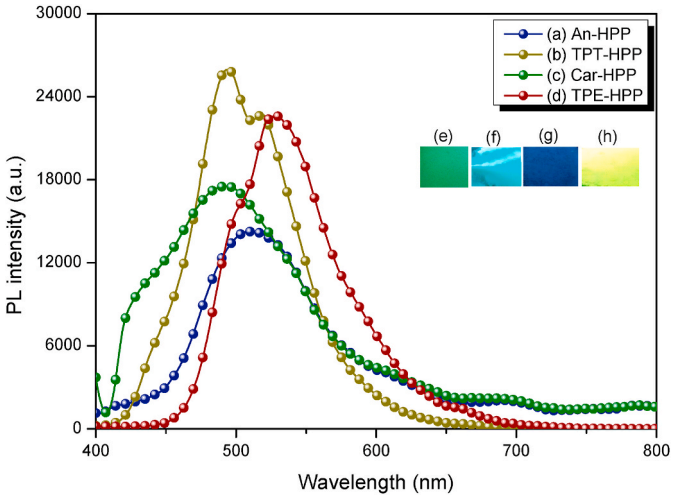

Fig. 8. Solid state PL spectra (excitation: 365 nm) of (a) An-HPP, (b) TPT-HPP, (c) Car-HPP, and (d) TPE-HPP. Photographs of (e) An-HPP, (f) TPT-HPP, (g) Car-HPP, and (h) TPE-HPP in the solid state under 365 nm UV illumination.

properties of our microporous polymers in the solid state and in solvents of various polarities. The UV–Vis absorption spectra (Fig. S10) of An-HPP, TPT-HPP, Car-HPP, and TPE-HPP each featured a broad absorption near 247 nm, attributed to their π–π* transitions. Fig. 8 displays the fluorescence emission spectra of An-HPP, TPT-HPP, Car-HPP and TPE-HPP in the solid state, with excitation at 365 nm. The spectrum of the anthracene-based microporous polymer An-HPP featured a broad emission peak at 512 nm; the maximum emission bands appeared at 494 and 519 nm for TPT-HPP, at 492 nm for Car-HPP, and at 528 nm for TPE-HPP. TPT-HPP and TPE-HPP exhibited higher fluorescence intensities and slightly red-shifted emissions when compared with An-HPP and Car-HPP.

We recorded the fluorescence spectra [Fig. 9(a–d)] of these microporous polymers in various solvents. The PL spectra recorded from THF, acetone, DMF, DMSO, and EtOH solutions featured emission peaks at 489, 498, 475, 480, and 472 nm, respectively, for An-HPP; at 492, 488, 479, 469, and 494 nm, respectively, for TPT-HPP; at 444, 433, 435, 431, and 439 nm, respectively, for Car-HPP; and at 520, 519, 517, 518, and 517 nm, respectively, for TPE-HPP. Thus, when the solvent polarity increased upon proceeding from THF to DMSO, the emission signals of An-HPP, TPT-HPP, and Car-HPP shifted from 482 to 500, from 478 to 490, and from 432 to 446 nm, respectively. Thus, these new materials exhibited solvatochromism, presumably because their π-conjugated structures and unfolded polymer backbones decreased the degree of chain aggregation [69–71]. Recently, Liu et al. prepared porous fluorescent polymers from flexible 2,4,6,8-tetramethyl-2,4,6,8-tetravinylcyclotetrasiloxanes and used them to detect Fe^{3+} ions and explosive materials [72].

Accordingly, we investigated the performance and selectivity of solutions of An-HPP, TPT-HPP, Car-HPP, and TPE-HPP in EtOH toward three different metal cations: Cu^{2+}, Fe^{2+}, Fe^{3+}, Mg^{2+}, Ni^{2+}, Zn^{2+}, and K^{+} [Fig. 10(a–d)]. As noted above, the fluorescence spectra of An-HPP, TPT-HPP, Car-HPP, and TPE-HPP in EtOH featured maximum broad emission peaks centered at 472, 494, 439, and 517 nm, respectively. After the addition of Cu^{2+} cations into solutions of these four microporous polymers, the PL emission intensities of An-HPP, TPT-HPP, and Car-HPP all decreased slightly, whereas emission quenching occurred in the case of TPE-HPP [Fig. 10(d)]. Upon the addition of Fe^{2+} and Fe^{3+}, the PL emission intensities of An-HPP, TPT-HPP, Car-HPP, and TPE-HPP were all quenched completely. As observed in Fig. 10(a–d), the PL emission intensities of An-HPP, TPT-HPP, Car-HPP, and TPE-HPP were increased upon the addition of Mg^{2+}, Ni^{2+} and Zn^{2+}. Upon the addition of K^{+} cation into An-HPP, TPT-HPP, Car-HPP, and TPE-HPP solution, the PL emission intensities of An-HPP, TPT-HPP and TPE-HPP all increased, whereas the PL emission intensity of Car-HPP decreased slightly.

In addition, we also examine the selectivity of solutions of An-HPP, TPT-HPP, Car-HPP, and TPE-HPP in EtOH toward aqueous solution of Fe^{3+} cation as presented in Fig. 11(a–d). Based on the experimental results, the luminescence intensity of An-HPP, TPT-HPP, Car-HPP, and TPE-HPP has a significant effect upon the addition different

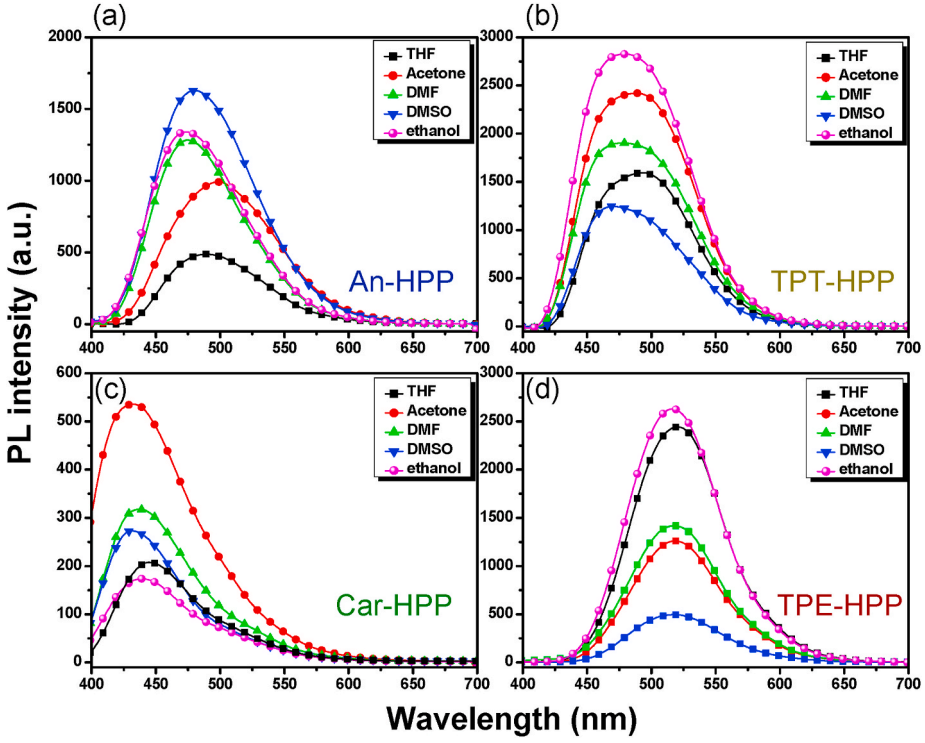

Fig. 9. PL spectra (excitation: 365 nm) of (a) An-HPP, (b) TPT-HPP, (c) Car-HPP, and (d) TPE-HPP in THF, acetone, DMF, DMSO, and EtOH.

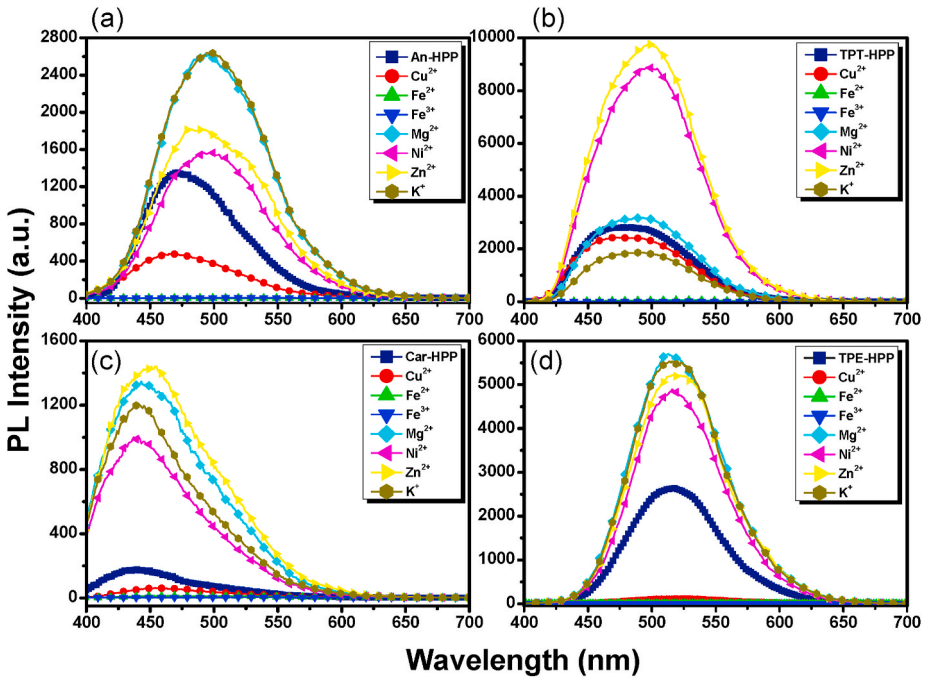

Fig. 10. PL spectra (excitation: 365 nm) of (a) An-HPP, (b) TPT-HPP, (c) Car-HPP, and (d) TPE-HPP in EtOH in the presence of Cu^{2+}, Fe^{2+}, Fe^{3+}, Mg^{2+}, Ni^{2+}, Zn^{2+}, and K^{+} cations.

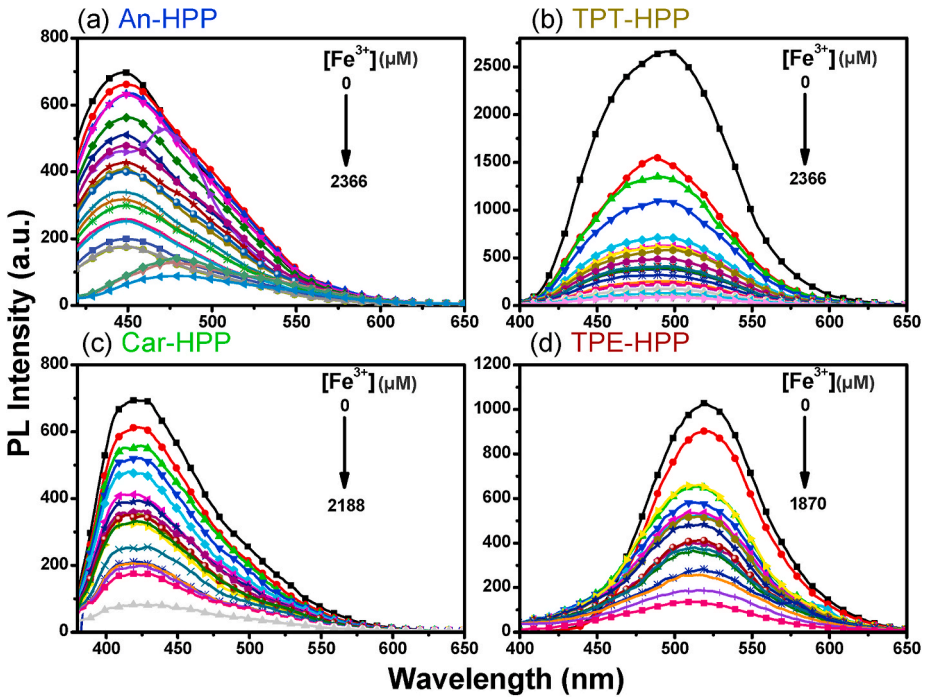

Fig. 11. Photoluminescence responses (excitation: 365 nm) of (a) An-HPP, (b) TPT-HPP, (c) Car-HPP, and (d) TPE-HPP sensor upon addition of Fe^{3+} cation.

concentration of Fe^{3+} solution. As observed from Fig. 11(a-d), the PL emission intensities of An-HPP, TPT-HPP and TPE-HPP decreased obviously and completely quenched when the increase the concentration of Fe^{3+} ions. Then, we estimated the quenching constant value (K_{SV}) by using Stern–Volmer equation: $I_0/I = 1 + K_{sv}[M]$; where I_0, I and M represents the PL intensity before Fe^{3+} addition, the luminous intensity after Fe^{3+} addition, and the molar concentration of Fe^{3+}, respectively. We found that the values of quenching constant (K_{SV}) [Fig. S11(a-d)] were 8.13×10^2, 5.69×10^3, 1.33×10^3 and 1.8×10^3 M^{-1} for An-HPP, TPT-HPP, Car-HPP, and TPE-HPP, respectively. Furthermore, the limit of detection (LOD) of An-HPP, TPT-HPP, Car-HPP, and TPE-HPP was calculated by using this equation: LOD = $3S/b$, where b is the slope of the calibration curve and S is the standard deviation of the fluorescence response. The LOD values were 46.0, 48.0, 229.0 and 138.0 μM for An-HPP, TPT-HPP, Car-HPP, and TPE-HPP. The association constant (K_a) of An-HPP, TPT-HPP, Car-HPP and TPE-HPP with Fe^{3+} cation was estimated using the standard Benesi-Hildebrand equation (1) [73,74].

$$\frac{Fmax - F_0}{F - F_0} = \frac{1}{[Fe^{3+}]^2 K_a} \quad (1)$$

where, F_0 is the fluorescence intensity of free sensor; F is the observed fluorescence intensity at any given concentration of Fe^{3+} in micromolar; F_{max} is the intensity at saturation point with the Fe^{3+}; and K_a is the association constant (M^{-2}). K_a was determined graphically by plotting $(F_{max} - F_0)/(F–F_0)$ *versus* $1/[Fe^{3+}]^2$ (Fig. S12). As shown in Fig. S12(a-d), The values of K_a were 2.09×10^5, 2.37×10^6, 4.98×10^5 and 8.78×10^6 M^{-2} for An-HPP, TPT-HPP, Car-HPP, and TPE-HPP, respectively.

4. Conclusion

We have synthesized four new POSS-based fluorescent HPPs—An-HPP, TPT-HPP, Car-HPP, and TPE-HPP through Heck reactions of a bulky POSS building block with the brominated monomers An-Br_2, TPT-Br_3, Car-Br_4, and TPE-Br_4 in the presence of $Pd(PPh_3)_4$. TGA revealed that An-HPP, TPT-HPP, Car-HPP, and TPE-HPP possessed thermal degradation temperatures and char yields higher than those of other previously reported organic FPPs, presumably because of the presence of rigid and bulky POSS units in the polymer frameworks. TPT-HPP and Car-HPP displayed excellent CO_2 uptake performance when compared with the other porous materials (Table S2). Finally, PL spectral measurements revealed that An-HPP, TPT-HPP, Car-HPP, and TPE-HPP could all act as chemical sensors for the metal cations Fe^{2+}, and Fe^{3+} in solution. Thus, HPPs such as these could be useful candidate materials for CO_2 adsorption and metal ion sensing.

Declaration of competing interest

The authors declare that they have no known competing financial interests or personal relationships that could have appeared to influence the work reported in this paper.

Acknowledgments

This study was supported financially by the Ministry of Science and Technology, Taiwan, under contracts MOST 106-2221-E-110- 067-MY3, 108-2638-E-002-003-MY2, and 108-2221-E-110-014-MY3.

Appendix ASupplementary data

Supplementary data to this article can be found online at https://doi.org/10.1016/j.micromeso.2020.110695.

References

[1] Y. Xu, S. Jin, H. Xu, A. Nagai, D. Jiang, Conjugated microporous polymers: design, synthesis and application, Chem. Soc. Rev. 42 (2013) 8012–8031.
[2] J.R. Holst, A. Trewin, A.I. Cooper, Porous organic molecules, Nat. Chem. 2 (2010) 915–920.
[3] J.S.M. Lee, T.H. Wu, B.M. Alston, M.E. Briggs, T. Hasell, C.C. Hub, A.I. Cooper, Porosity-engineered carbons for supercapacitive energy storage using conjugated microporous polymer precursor, J. Mater. Chem. 4 (2016) 7665–7673.
[4] M.G. Mohamed, E.C.A. Jr, B.M. Matsagar, J. Na, Y. Yamauchi, K.C.W. Wu, S. W. Kuo, Construction hierarchically mesoporous/microporous materials based on block copolymer and covalent organic framework, J. Taiwan. Inst. Chem. Eng. 112 (2020) 180–192.
[5] D. Wang, L. Li, W. Yang, Y. Zuo, S. Feng, H. Liu, POSS-based luminescent porous polymers for carbon dioxide sorption and nitroaromatic explosives detection, RSC Adv. 4 (2014) 59877–59884.
[6] J. Tang, R.R. Salunkhe, H. Zhang, V. Malgras, T. Ahamad, S.M. Alshehri, N. Kobayashi, S. Tominaka, Y. Ide, J.H. Kim, Y. Yamauchi, Bimetallic metal-organic frameworks for controlled catalytic graphitization of nanoporous carbons, Sci. Rep. 6 (2016) 30295.
[7] Y.V. Kaneti, J. Zhang, Y.B. He, Z. Wang, S. Tanaka, M.S.A. Hossain, Z.Z. Pan, B. Xiang, Q.H. Yang, Y. Yamauchi, Fabrication of an MOF-derived heteroatom-doped Co/CoO/carbon hybrid with superior sodium storage performance for sodium-ion batteries, J. Mater. Chem. 5 (2017) 15356.
[8] T. Ben, H. Ren, S.Q. Ma, D.P. Cao, J.H. Lan, X.F. Jing, W.C. Wang, J. Xu, F. Deng, J. M. Simmons, S.L. Qiu, G.S. Zhu, Targeted synthesis of a porous aromatic framework with high stability and exceptionally high surface area, Angew. Chem. Int. Ed. 48 (2009) 9457–9460.
[9] K.I. Aly, M.M. Sayed, M.G. Mohamed, S.W. Kuo, O. Younis, A facile synthetic route and dual function of network luminescent porous polyester and copolyester containing porphyrin moiety for metal ions sensor and dyes adsorption, Microporous Mesoporous Mater. 298 (2020) 110063.
[10] H. Liu, H. Liu, Selective dye adsorption and metal ion detection using multifunctional silsesquioxane-based tetraphenylethene-linked nanoporous polymers, J. Mater. Chem. 5 (2017) 9156–9162.
[11] C. Zhang, P. Zhu, L. Tan, J. Liu, B. Tan, X. Yang, H. Xu, Triptycene-based hyper-cross-linked polymer sponge for gas storage and water treatment, Macromolecules 48 (2015) 8509–8514.
[12] Y.V. Kaneti, S. Dutta, M.S.A. Hossain, M.J.A. Shiddiky, K.L. Tung, F.K. Shieh, C. K. Tsung, K.C.W. Wu, Y. Yamauchi, Strategies for improving the functionality of zeolitic imidazolate frameworks: tailoring nanoarchitectures for functional applications, Adv. Mater. 29 (2017) 1700213.
[13] C. Wang, J. Kim, J. Tang, J. Na, Y.M. Kang, M. Kim, H. Lim, Y. Bando, J. Li, Y. Yamauchi, Large-scale synthesis of MOF-derived superporous carbon aerogels with extraordinary adsorption capacity for organic solvents, Angew. Chem. Int. Ed. 59 (2020) 2066.
[14] C. Wang, J. Kim, J. Tang, M. Kim, H. Lim, V. Malgras, J. You, Q. Xu, J. Li, Y. Yamauchi, New strategies for novel MOF-derived carbon materials based on nanoarchitectures, Chem. 6 (2020) 19–40.
[15] M.G. Mohamed, X. Zhang, T.H. Mansoure, A.F.M. EL-Mahdy, C.F. Huang, M. Danko, Z. Xin, S.W. Kuo, Hypercrosslinked porous organic polymers based on tetraphenyl anthraquinone for CO_2 uptake and high-performance supercapacitor, Polymer 205 (2020) 122857.
[16] C.H. Christensen, K. Johannsen, I. Schmidt, C.H. Christensen, Catalytic benzene alkylation over mesoporous zeolite single Crystals: improving activity and selectivity with a new family of porous materials, J. Am. Chem. Soc. 125 (2003) 13370–13371.
[17] P. Wu, J. Wang, C. He, X. Zhang, Y. Wang, T. Liu, C. Duan, Luminescent metal-organic frameworks for selectively sensing nitric oxide in an aqueous solution and in living cells, Adv. Funct. Mater. 22 (2012) 1698–1703.
[18] M.G. Mohamed, A.F.M. EL-Mahdy, Y. Takashi, S.W. Kuo, Ultrastable conductive microporous covalent triazine frameworks based on pyrene moieties provide high-performance CO_2 uptake and supercapacitance, New J. Chem. 44 (2020) 8241–8253.
[19] A.F.M. EL-Mahdy, A.M. Elewa, S.W. Huang, H.H. Chou, S.W. Kuo, Dual-Function fluorescent covalent organic frameworks: HCl sensing and photocatalytic H_2 evolution from water, Adv. Optical Mater. 8 (2020) 2000641.
[20] P. Wu, J. Wang, Y. Li, C. He, Z. Xie, C. Duan, Luminescent sensing and catalytic performances of a multifunctional lanthanide-organic framework comprising a triphenylamine moiety, Adv. Funct. Mater. 21 (2011) 2788–2794.
[21] R.E. Morris, P.S. Wheatley, Gas storage in nanoporous materials, Angew. Chem. Int. Ed. 47 (2008) 4966–4981.
[22] M.G. Mohamed, A.F.M. EL-Mahdy, M.M.M. Ahmed, S.W. Kuo, Direct synthesis of microporous bicarbazole-based covalent triazine frameworks for high-performance energy storage and carbon dioxide uptake, ChemPlusChem 84 (2019) 1767–1774.
[23] H.L. Qian, C. Dai, C.X. Yang, X.P. Yan, High-crystallinity covalent organic framework with dual fluorescence emissions and its ratiometric sensing application, ACS Appl. Mater. Interfaces 9 (2017) 24999–25005.
[24] A.F.M. EL-Mahdy, M.G. Mohamed, T.H. Mansoure, H.H. Yu, T. Chen, S.W. Kuo, Ultrastable tetraphenyl-p-phenylenediamine-based covalent organic frameworks as platforms for high-performance electrochemical supercapacitors, Chem. Commun. 55 (2019) 14890–14893.
[25] Z. Yang, J. Han, R. Jiao, H. Sun, Z. Zhu, W. Liang, A. Li, Porous carbon framework derived from N-rich hypercrosslinked polymer as the efficient metal-free electrocatalyst for oxygen reduction reaction, J. Colloid Interface Sci. 557 (2019) 664–672.
[26] H. Wang, B. Li, H. Wu, T. Hu, Z. Yao, W. Zhou, S. Xiang, B. Chen, A flexible microporous hydrogen-bonded organic framework for gas sorption and separation, J. Am. Chem. Soc. 137 (2015) 9963–9970.
[27] M.G. Mohamed, C.C. Lee, A.F.M. EL-Mahdy, J. Luder, M.H. Yu, Z. Li, Z. Zhu, C. C. Chueh, S.W. Kuo, Exploitation of two-dimensional conjugated covalent organic frameworks based on tetraphenylethylene with bicarbazole and pyrene units and applications in perovskite solar cells, J. Mater. Chem. A 8 (2020) 11448–11459.
[28] L. Hu, S. Gu, W. Yu, W. Zhang, Q. Xie, C. Pan, J. Tang, G. Yu, Facile preparation of CoO nanoparticles embedded N-doped porous carbon from conjugated microporous polymer for oxygen reduction reaction, J. Colloid Interface Sci. 562 (2020) 550–557.
[29] A.F.M. EL-Mahdy, C.H. Kuo, A. Alshehri, C. Young, Y. Yamauchi, J. Kim, S.W. Kuo, Strategic design of triphenylamine- and triphenyltriazine-based two-dimensional covalent organic frameworks for CO_2 uptake and energy storage, J. Mater. Chem. A 6 (2018) 19532–19541.
[30] Y. Yuan, H. Ren, F. Sun, X. Jing, K. Cai, X. Zhao, Y. Wang, Y. Wei, G. Zhu, Targeted synthesis of a 3D crystalline porous aromatic framework with luminescence quenching ability for hazardous and explosive molecules, J. Phys. Chem. C 116 (2012) 26431–26435.
[31] D. Chen, C. Liu, J. Tang, L. Luo, G. Yu, Fluorescent porous organic polymers, Polym. Chem. 10 (2019) 1168–1181.
[32] S. Wan, J. Guo, J. Kim, H. Ihee, D. Jiang, A photoconductive covalent organic framework: self-condensed arene cubes composed of eclipsed 2D polypyrene sheets for photocurrent generation, Angew. Chem. Int. Ed. 48 (2009) 5439–5442.

[33] A.F.M. EL-Mahdy, M.Y. Lai, S.W. Kuo, A highly fluorescent covalent organic framework as a hydrogen chloride sensor: roles of Schiff base bonding and π-stacking, J. Mater. Chem. C 8 (2020) 9520–9528.
[34] Q. Chen, J. Wang, F. Yang, D. Zhou, N. Bian, X. Zhang, C. Yan, B. Han, Tetraphenylethylene-based fluorescent porous organic polymers: preparation, gas sorption properties and photoluminescence properties, J. Mater. Chem. 21 (2011) 13554–13560.
[35] J.X. Jiang, A. Trewin, D.J. Adams, A.I. Cooper, Band gap engineering in fluorescent conjugated microporous polymers, Chem. Sci. 2 (2011) 1777–1781.
[36] Y.H. Xu, L. Chen, Z.Q. Guo, A. Nagai, D.L. Jiang, Light-emitting conjugated polymers with microporous network architecture: interweaving scaffold promotes electronic conjugation, facilitates exciton migration, and improves luminescence, J. Am. Chem. Soc. 133 (2011) 17622–17625.
[37] X.M. Liu, Y.H. Xu, D.L. Jiang, Conjugated microporous polymers as molecular sensing devices: microporous architecture enables rapid response and enhances sensitivity in fluorescence-on and fluorescence-off sensing, J. Am. Chem. Soc. 134 (2012) 8738–8741.
[38] M.G. Mohamed, S.W. Kuo, Functional polyimide/polyhedral oligomeric silsesquioxane nanocomposites, Polymers 11 (2019) 26.
[39] M.G. Mohamed, S.W. Kuo, Functional silica and carbon nanocomposites based on polybenzoxazines, Macromol. Chem. Phys. 220 (2019) 1800306.
[40] Z. Liu, S. Ma, L. Chen, J. Xu, J. Ou, M. Ye, Porous styryl-linked polyhedral oligomeric silsesquioxane (POSS) polymers used as a support for platinum catalysts, Mater. Chem. Front. 3 (2019) 851–859.
[41] M.G. Mohamed, K.C. Hsu, J.L. Hong, S.W. Kuo, Unexpected fluorescence from maleimide-containing polyhedral oligomeric silsesquioxanes: nanoparticle and sequence distribution analyses of polystyrene-based alternating copolymers, Polym. Chem. 7 (2016) 135–145.
[42] M.G. Mohamed, S.W. Kuo, Polybenzoxazine/polyhedral oligomeric silsesquioxane (POSS) nanocomposites, Polymers 8 (2016) 225.
[43] S.W. Kuo, F.C. Chang, POSS related polymer nanocomposites, Prog. Polym. Sci. 36 (2011) 1649–1696.
[44] W.C. Chen, M.M.M. Ahmed, C.F. Wang, C.F. Huang, S.W. Kuo, Highly thermally stable mesoporous Poly (cyanate ester) featuring double-decker–shaped polyhedral silsesquioxane framework, Polymer 185 (2019) 121940.
[45] D. Wang, W. Yang, S. Feng, H. Liu, Amine post-functionalized POSS-based porous polymers exhibiting simultaneously enhanced porosity and carbon dioxide adsorption properties, RSC Adv. 6 (2016) 13749–13756.
[46] W.C. Chen, S.W. Kuo, Ortho-imide and allyl groups effect on highly thermally stable polybenzoxazine/double-decker-shaped polyhedral silsesquioxane hybrids, Macromolecules 51 (2018) 9602–9612.
[47] H.K. Shih, C.C. Hsieh, M.G. Mohamed, C.Y. Zhu, S.W. Kuo, Ternary polybenzoxazine/POSS/SWCNT hybrid nanocomposites stabilized through supramolecular interactions, Soft Matter 12 (2016) 1847–1858.
[48] X. Zhang, S. Zhao, M.G. Mohamed, S.W. Kuo, Z. Xin, Crystallization behaviors of poly (ethylene terephthalate) (PET) with monosilane isobutyl-polyhedral oligomeric silsesquioxanes (POSS), J. Mater. Sci. 55 (2020) 14642–14655.
[49] L. Sun, Z. Liang, J. Yu, Octavinylsilsesquioxane-based luminescent nanoporous inorganic–organic hybrid polymers constructed by the Heck coupling reaction, Polym. Chem. 6 (2015) 917–924.
[50] G. Chen, Y. Zhou, X. Wang, J. Li, S. Xue, Y. Liu, Q. Wang, J. Wang, Construction of porous cationic frameworks by crosslinking polyhedral oligomeric silsesquioxane units with N-heterocyclic linkers, Sci. Rep. 5 (2015) 11236.
[51] H. Liu, M. Ge, A silsesquioxane-based thiophene-bridged hybrid nanoporous network as a highly efficient adsorbent for wastewater treatment, J. Mater. Chem. 4 (2016) 16714–16722.
[52] D. Wang, W. Yang, S. Feng, H. Liu, Constructing hybrid porous polymers from cubic octavinyl silsequioxane and planar halogenated benzene, Polym. Chem. 5 (2014) 3634–3642.
[53] X. Jing, F. Sun, H. Ren, Y. Tian, M. Guo, L. Li, G. Zhu, Targeted synthesis of micro–mesoporous hybrid material derived from octaphenylsilsesquioxane building units, Microporous Mesoporous Mater. 165 (2013) 92–98.
[54] W. Chaikittisilp, A. Sugawara, A. Shimojima, T. Okubo, Hybrid porous materials with high surface area derived from bromophenylethenyl-functionalized cubic siloxane-based building units, Chem. Eur J. 16 (2010) 6006–6014.
[55] L. Zhang, H.C.L. Abbenhuis, Q. Yang, Y.M. Wang, P.C.M.M. Magusin, B. Mezari, R. A. van Santen, C. Li, Mesoporous organic–inorganic hybrid materials built using polyhedral oligomeric silsesquioxane blocks, Angew. Chem. Int. Ed. 46 (2007) 5003–5006.
[56] H. Yang, H. Liu, Pyrene-functionalized silsesquioxane as fluorescent nanoporous material for antibiotics detection and removal, Microporous Mesoporous Mater. 300 (2020) 110135.
[57] T. Geng, C. Zhang, G. Chen, L. Ma, W. Zhang, H. Xia, Synthesis of tetraphenylethylene-based fluorescent conjugated microporous polymers for fluorescent sensing and adsorbing iodine, Microporous Mesoporous Mater. 284 (2019) 468–475.
[58] D. Wang, S. Feng, H. Liu, Fluorescence-tuned polyhedral oligomeric silsesquioxane-based porous polymers, Chem. Eur J. 22 (2016) 14319–14327.
[59] R.S. Sprick, J.X. Jiang, B. Bonillo, S. Ren, T. Ratvijitvech, P. Guiglion, M. A. Zwijnenburg, D.J. Adams, A.I. Cooper, Tunable organic photocatalysts for visible-light-driven hydrogen evolution, J. Am. Chem. Soc. 137 (2015) 3265–3270.
[60] D. Wang, L. Xue, L. Li, B. Deng, S. Feng, H. Liu, X. Zhao, Rational design and synthesis of hybrid porous polymers derived from polyhedral oligomeric silsesquioxanes via Heck coupling reactions, macro, Rapid Commun 34 (2013) 861–866.
[61] M. Soldatov, H. Liu, A POSS-phosphazene based porous material for adsorption of metal ions from water, Chem. Asian J. 14 (2019) 4345.
[62] D. Wang, W. Yang, L. Li, X. Zhao, S. Feng, H. Liu, Hybrid networks constructed from tetrahedral silicon-centered precursors and cubic POSS-based building blocks via Heck reaction: porosity, gas sorption, and luminescence, J. Mater. Chem. 1 (2013) 13549–13558.
[63] M.F. Roll, J.W. Kampf, Y. Kim, E. Yi, R.M. Laine, Nano building blocks via iodination of $[PhSiO_{1.5}]_n$, forming $[p\text{-}I\text{-}C_6H_4SiO_{1.5}]_n$ (n = 8, 10, 12), and a new route to high-surface-area, thermally stable, microporous materials via thermal elimination of I_2, J. Am. Chem. Soc. 132 (2010) 10171–10174.
[64] J.Y. Wu, M.G. Mohamed, S.W. Kuo, Directly synthesized nitrogen-doped microporous carbons from polybenzoxazine resins for carbon dioxide capture, Polym. Chem. 8 (2017) 5481–5489.
[65] M.G. Mohamed, S.M. Ebrahium, A.S. Hammam, S.W. Kuo, K.I. Aly, Enhanced CO_2 capture in nitrogen-enriched microporous carbons derived from Polybenzoxazines containing azobenzene and carboxylic acid units, J. Polym. Res. 27 (2020) 197.
[66] M.G. Mohamed, M.Y. Tsai, W.C. Su, A.F.M. EL-Mahdy, C.F. Wang, C.F. Huang, L. Dai, T. Chen, S.W. Kuo, Nitrogen-Doped microporous carbons derived from azobenzene and nitrile-functionalized polybenzoxazines for CO_2 uptake, Mater. Today Commun. 24 (2020) 101111.
[67] R. Dawson, E. Stöckel, J.R. Holst, D.J. Adams, A.I. Cooper, Microporous organic polymers for carbon dioxide capture, Energy Environ. Sci. 4 (2011) 4239.
[68] S. Ren, R. Dawson, A. Laybourn, J. Jiang, Y. Khimyak, D.J. Adamsa, A.I. Cooper, Functional conjugated microporous polymers: from 1,3,5-benzene to 1,3,5-triazine, Polym. Chem. 3 (2012) 928–934.
[69] K.V. Rao, R. Haldar, T.K. Maji, S.J. George, Dynamic, conjugated microporous polymers: visible light harvesting via guest-responsive reversible swelling, Phys. Chem. Chem. Phys. 18 (2016) 156–163.
[70] M.G. Mohamed, Y.R. Jheng, S.L. Yeh, T. Chen, S.W. Kuo, Unusual emission of polystyrene-based alternating copolymers incorporating aminobutyl maleimide fluorophore-containing polyhedral oligomeric silsesquioxane nanoparticles, Polymers 9 (2017) 103.
[71] S. Hayashi, Y. Togawa, S.I. Yamamoto, T. Koizumi, K. Nishi, A. Asano, Synthesis of π-conjugated network polymers based on fluoroarene and fluorescent units via direct arylation polycondensation and their porosity and fluorescent properties, J. Polym. Sci., Part A: Polym. Chem. 55 (2017) 3862–3867.
[72] R. Sun, S. Feng, B. Zhou, Z. Chen, D. Wang, H. Liu, Flexible cyclosiloxane-linked fluorescent porous polymers for multifunctional chemical sensors, ACS Macro Lett. 9 (2020) 43–48.
[73] M. Ahumada, E. Lissi, A.M. Montagut, F.V. Henriquez, N.L. Pacioni, E.I. Alarcon, Association models for binding of molecules to nanostructures, Analyst 142 (2017) 2067–2089.
[74] Y. Li, J. Wu, X. Jin, J. Wang, S. Han, W. Wu, J. Xu, W. Liu, X. Yao, Y. Tang, A bimodal multianalyte simple molecule chemosensor for Mg^{2+}, Zn^{2+}, and Co^{2+}, Dalton Trans. 43 (2014) 1881–1887.